Journal of Materials Chemistry A

ROYAL SOCIETY OF CHEMISTRY

PAPER

View Article Online
View Journal | View Issue

Cite this: J. Mater. Chem. A, 2025, 13, 31740

Reproducible synthesis of α-MgAgSb with optimized carrier transport for low-temperature thermoelectric applications

Saba Sepahban Shahgoli, †[ab] Melis Ozen, †[abc] Duncan Zavanelli, [d] Gulchin Aliyeva, [b] Arda Baran Burcak, [b] Ulrich Burkhardt, [e] Eleonora Isotta, [d] G. Jeffrey Snyder [d] and Umut Aydemir *[bf]

Developing reproducible, high-performance thermoelectric (TE) materials for cooling and low-grade heat recovery applications remains a pressing challenge, particularly for tellurium-free systems. In this study, we systematically optimize the synthesis of α-MgAgSb *via* two-step ball milling, spark plasma sintering (SPS), and targeted post-annealing. We demonstrate that sintering at 673 K, followed by a 3-days annealing period and an additional low-temperature stabilization step, yields $MgAg_{0.97}Sb$ samples with minimal secondary phases, high TE performance and excellent reproducibility. The optimized materials achieve a maximum zT of 0.84 near room temperature and reach 1.3 at 500 K, placing them among the highest-performing Te-free p-type TE materials reported to date. These significant enhancements are attributed to improved Hall mobility (μ ~130 $cm^2\ V^{-1}\ s^{-1}$), minimized secondary-phase content, and suppressed thermal conductivity (κ). Further analyses using weighted mobility (μ_w) and the TE quality factor (B) confirm that the carrier concentration (n) closely approaches the theoretical optimum, providing strong alignment between experimental and predicted zT values. This research establishes a robust and scalable synthesis protocol, highlighting α-MgAgSb as a highly promising candidate for sustainable, efficient, and practical low-temperature TE module applications.

Received 30th June 2025
Accepted 11th August 2025

DOI: 10.1039/d5ta05284j

rsc.li/materials-a

1 Introduction

Harnessing waste heat, which accounts for over 60% of global energy losses, represents a key opportunity for improving energy efficiency and reducing carbon emissions.[1] Low-grade waste heat (<573 K) is especially challenging to recover using conventional systems like Rankine and Stirling cycles, which show limited performance for small temperature differentials and low energy density.[2] The TE technology, however, offers a sustainable alternative, directly converting heat into electricity through a solid-state mechanism that requires no moving parts or maintenance while producing zero emissions.[3–5] TE devices also serve as eco-friendly cooling systems, providing carbon-free alternatives to conventional refrigeration. These systems have several advantages over traditional cooling methods, including compact size, lightweight design, high reliability, and the absence of working fluids. Due to these benefits, TE cooling technology is gaining interest for applications in various fields, such as electronic cooling for PC processors, portable food and beverage storage, temperature-controlled car seats, and TE air conditioners.[6] The performance of TE materials is characterized by the dimensionless TE figure-of-merit, zT, which depends on the material's Seebeck coefficient (S), electrical conductivity (σ), and κ at absolute temperature (T) and is defined as: $zT = \frac{S^2\sigma}{\kappa}T$. Achieving a high zT requires an optimal balance between these interdependent transport properties, which necessitates a thorough examination of how changes in the synthesis process influence TE properties.[5] One critical aspect is the enhancement of the power factor ($PF = S^2\sigma$), which directly contributes to improved electrical performance. Simultaneously, the phonon-glass electron-crystal (PGEC) concept has been crucial in advancing TE materials.[7] This approach focuses on engineering materials that behave like glass for phonons, thereby minimizing κ, while retaining crystal-like properties to enhance σ. The PGEC concept has been a key driving force behind the development of high-performance TE materials,[8] enabling significant improvements in zT by decoupling the electronic and thermal transport properties.

[a]Graduate School of Sciences and Engineering, Koç University, Istanbul-34450, Türkiye
[b]Koç University Boron and Advanced Materials Application and Research Center (KUBAM), Istanbul-34450, Türkiye. E-mail: uaydemir@ku.edu.tr
[c]Turkish Aerospace, Fethiye District, Havacilik Avenue No:17 06980 Kahramankazan, Ankara, Türkiye
[d]Department of Materials Science and Engineering, Northwestern University, Evanston, IL-60208, USA
[e]Max-Planck-Institut für Chemische Physik fester Stoffe, Dresden-01187, Germany
[f]Department of Chemistry, Koç University, Sariyer, Istanbul-34450, Türkiye
† Authors (S.S.S. and M.O.) contributed equally to this article.

Over recent decades, substantial efforts to enhance zT have led to notable improvements in several TE families of compounds. These include, but are not limited to, Bi_2Te_3,[9,10] skutterudites,[11,12] lead chalcogenides,[13] half-Heuslers,[14] Zintls,[15,16] SiGe alloys,[17] and IV–VI compounds,[18] achieving zT values exceeding 1, particularly at high temperatures. These advances have been primarily driven by strategies such as doping, alloying, band and grain boundary engineering, and nanostructuring.[19] Despite these advancements, commercial TE applications for cooling and low-temperature waste heat recovery (<573 K) have been dominated by bismuth telluride (Bi_2Te_3) and its derivatives for over half a century, typically achieving conversion efficiencies of ~3–6%.[20–22] However, the poor mechanical properties and reliance on tellurium, a scarce and increasingly expensive element, have spurred the search for alternative materials that can deliver comparable performance but with fewer environmental concerns[23–25] and p-type α-MgAgSb[26–30] have garnered substantial interest as a promising low-temperature material, offering zT values near 1.0 at temperatures below 550 K, along with favorable mechanical properties, elemental abundance, and non-toxicity. N-type Mg_3Sb_2 derivatives serve as the primary counterparts to p-type α-MgAgSb; yet, despite both possessing attractive TE characteristics, α-MgAgSb usually delivers lower overall performance. $Mg_3(Bi,Sb)_2$ stands out for its adherence to the PGEC concept, exhibiting inherently low κ alongside favorable electronic transport properties. Recent studies have demonstrated impressive TE performance in both n-type $Mg_3(Bi,Sb)_2$ materials and their modules.[31–39] The intrinsic low lattice thermal conductivity (κ_l) of α-MgAgSb, a key determinant of its high TE efficiency, arises from a complex interplay of factors including complex crystal structure, beneficial lattice dynamics properties, intrinsic Ag vacancies, and multiscale microstructures, which suppress thermal transport while maintaining good σ.[39] However, the α–β–γ phase transitions in MgAgSb occurring near 320–420 °C,[26] as well as the occurrence of other impurity phases such as Ag_3Sb, Sb, or Mg_3Sb_2,[26,40–42] make it difficult to achieve phase-pure α-MgAgSb using traditional synthesis methods. For example, Kirkham *et al.* synthesized α-MgAgSb using vacuum-melting followed by hot-press sintering but detected significant amounts of secondary phases (Sb and Ag_3Sb), limiting zT to ~0.55 at 423 K.[26] Numerous studies have aimed to improve the performance of α-MgAgSb by employing various methods to obtain pure, high-performance samples including melting with subsequent annealing,[26,28] ball milling followed by sintering and annealing,[40] and microwave-assisted melting.[43] Zhao *et al.* achieved the best results to date by implementing a novel two-step ball milling process followed by sintering.[29] The composition was refined from MgAgSb to $MgAg_{0.97}Sb_{0.99}$, resulting in nanostructured samples free from detectable impurity phases and yielding a maximum zT of approximately 0.7 at 300 K and 1.2 at 450 K. Further efforts to optimize composition, stabilize phases, and incorporate doping and defect engineering have yielded promising zT values, comparable to or exceeding those of traditional Bi_2Te_3-based materials.[44–49] Among these, Ni doping at the Ag lattice site achieved the highest zT, nearing 1 at room temperature and ~1.4 at 450 K.[29] Building on this progress, a recent study examined the effects of different ball milling strategies on α-MgAgSb, focusing on its structure and transport properties.[50] Optimized milling suppressed Ag_3Sb impurities, increasing grain size, μ, and PF. A peak zT of 1.36 at 473 K was achieved for a refined composition of $MgAg_{0.97}Sb_{0.99}$, highlighting the importance of microstructural control in enhancing TE performance.

In parallel, the integration of MgAgSb into TE modules, using $Mg_3(Sb,Bi)_2$ as an n-type counterpart, has demonstrated remarkable efficiency gains. Notably, Kraemer's group used a simple one-step hot-pressing method to fabricate a single α-MgAgSb leg with silver pads, achieving ~8.5% efficiency at a 225 K temperature difference (ΔT).[51] Liu *et al.* successfully fabricated an 8-pair TE module consisting of p-type $Mg_{0.99}Cu_{0.01}Ag_{0.97}Sb_{0.99}$ and n-type $Mg_{3.2}Sb_{1.5}Bi_{0.49}Te_{0.01}Cu_{0.01}$, reaching ~7.3% efficiency at a hot-side temperature of 593 K.[34] Ying *et al.* initially reported a conversion efficiency of 6.5% for a temperature difference of 250 K.[52] In their most recent work, they have demonstrated that n-type $Mg_{3.6}Y_{0.003}Sb_{0.6}Bi_{1.4}$ together with p-type $MgAg_{0.97}Sb_{0.99}$ achieved module-level conversion efficiencies of 8.5% under ΔT of 260 K.[53] A recent study further demonstrated 12% efficiency near room temperature using p-type α-MgAgSb and n-type $Mg_{3.285}Nb_{0.015}SbBi_{0.9975}Te_{0.0035}$, with a hot-side temperature of 583 K and ΔT of 61 K.[54]

To establish α-MgAgSb as a reliable module material, it is crucial not only to optimize its TE performance but also to reproducibly achieve consistent transport results through scalable synthesis methods.[55] Despite the progress in synthesis techniques, reproducibility of TE properties of MgAgSb remains a major challenge, underscoring the need for robust fabrication processes. This study focuses on the development and optimization of α-MgAgSb for low-temperature TE applications. By incorporating additional heat treatment and carefully tuning the sintering temperatures, we improved the synthesis process to consistently yield high-quality materials. As a result, our samples exhibited reproducible TE performance, with a maximum zT of 0.84 near room temperature and up to 1.3 at 500 K. Notably, as-prepared materials display exceptionally high μ, reaching ~130 $cm^2\ V^{-1}\ s^{-1}$ at room temperature, which reflects the effectiveness of our optimized processing strategy. These results highlight the strong potential of MgAgSb-based materials for efficient and environmentally friendly TE module applications.

2 Experimental section

2.1 Sample preparation

The target materials were synthesized using a two-stage ball milling process with high-purity magnesium powder (Mg, 99.8%; Alfa Aesar), micron-sized silver powder (Ag, 99.99%; Nanografi Nano Technology), and antimony shots (Sb, 99.999%; Alfa Aesar). To prevent side reactions caused by the high reactivity of elements during high-energy ball milling and to avoid oxidation of the chemicals, all sample preparation steps were conducted in an Ar-filled glovebox.

In the first stage, the binary phase $MgAg_{0.97}$ was prepared by loading stoichiometric amounts of Mg and Ag into a stainless-steel vial with two half-inch stainless steel balls. The vial was then sealed inside the glovebox to maintain an inert atmosphere. Mechanochemical synthesis was performed in a high-energy ball mill (SPEX 8000M Mixer/Mill, 1425 rpm) for 8 hours to ensure thorough mixing and sample homogeneity. In the second stage, the stoichiometric amount of Sb was added to the milled mixture in the glovebox. This was followed by a second round of high-energy milling, which was carried out for 5 hours. The two-step ball milling process is schematically illustrated in Fig. 1a, showing the sequential addition of elements to produce the final $MgAg_{0.97}Sb$ powder.

To consolidate the samples with SPS, the ball-milled powder was loaded into a graphite die inside the glovebox. The SPS process was performed for 8 minutes at a pressure of 80 MPa at two different temperatures of 573 K and 673 K. The resulting pellets were then sealed in quartz ampoules under vacuum and subjected to heat treatment in a furnace at 553 K for durations of 3 days.

To minimize discrepancies in electronic transport measurements during heating and cooling cycles, an additional heat treatment step was introduced. This process involved heating the sample to 573 K over 4.5 h, holding it at this temperature for 10 minutes, and then allowing it to cool gradually to room temperature in 3 h, as described in the subsequent sections. Fig. 1b schematically presents the subsequent steps, including SPS and post-annealing treatments.

2.2 Sample characterization

The phase purity of the samples was assessed using X-ray diffraction (XRD) with a Rigaku MiniFlex 600 ($CuK_\alpha = 1.5418$ Å, 40 kV, 15 mA). Measurements were performed on both powder and bulk samples to ensure comprehensive analysis. Microstructure analyses were conducted using scanning electron microscopy (SEM, JEOL JSM 7800F field emission cathode) equipped with an Energy Dispersive X-ray system (EDS; silicon drift detector (SDD), Quantax 400, Brukernano, Berlin). Phase transition temperatures were determined using differential scanning calorimetry (DSC, NETZSCH STA 449 F3 Jupiter).

The microhardness measurements were performed with a Shimadzu Micro Hardness Tester HMV-G21, applying a load of 2.94 N. Results were averaged from 8 selected spots. The Vickers hardness (Hv) was calculated by using the formula $Hv = 1.8544\frac{F_0}{d^2}$, where F_0 is the applied load and d is the diagonal length of the indentation impression.

2.3 Transport properties measurements

To measure the thermal transport properties, sintered samples in the form of 1 mm-thick discs with a diameter of 10 mm were used. For electronic transport measurements, bar-shaped samples with a minimum thickness of 2.5 mm were prepared by cutting with a low-speed diamond-wire saw (WELL 3500). κ was calculated using the formula $\kappa = D \times C_p \times d$, where D is the thermal diffusivity, C_p is the heat capacity, and d is the experimental density of the sample. Disc-shaped samples were placed

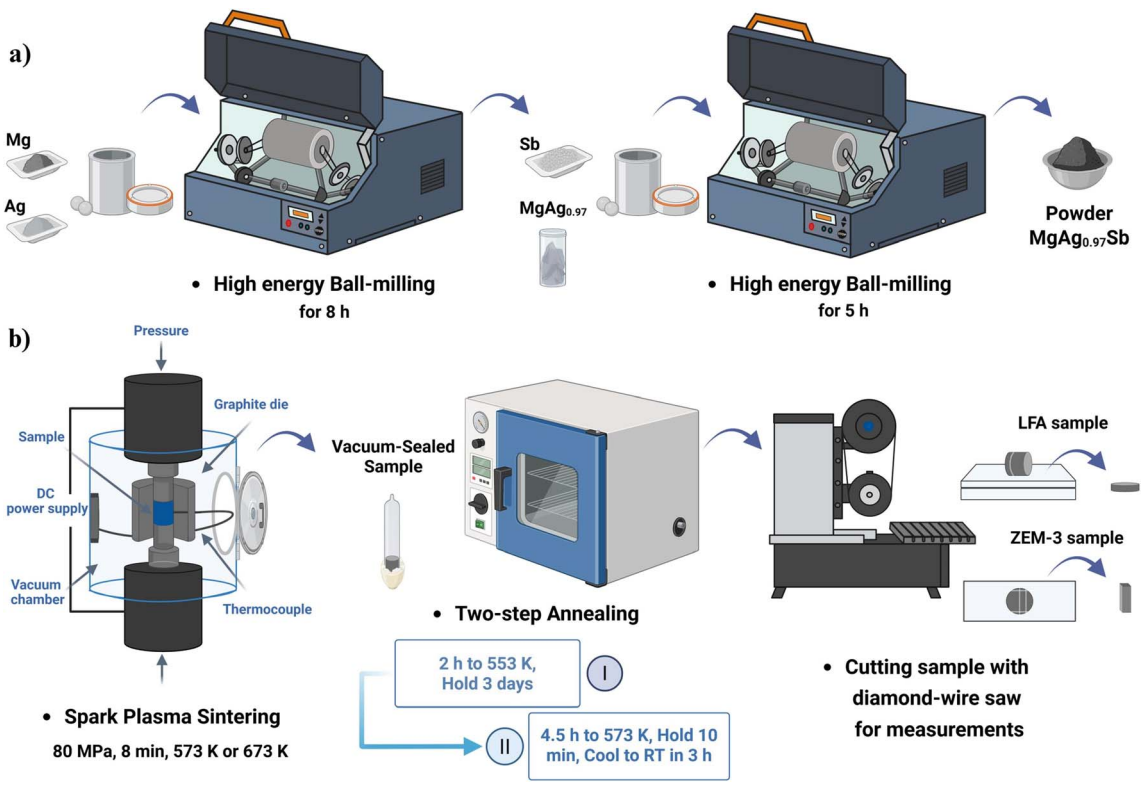

Fig. 1 Schematic of the synthesis and characterization process for $MgAg_{0.97}Sb$, including (a) two-step ball milling, and (b) SPS, annealing, and sample preparation for TE measurements.

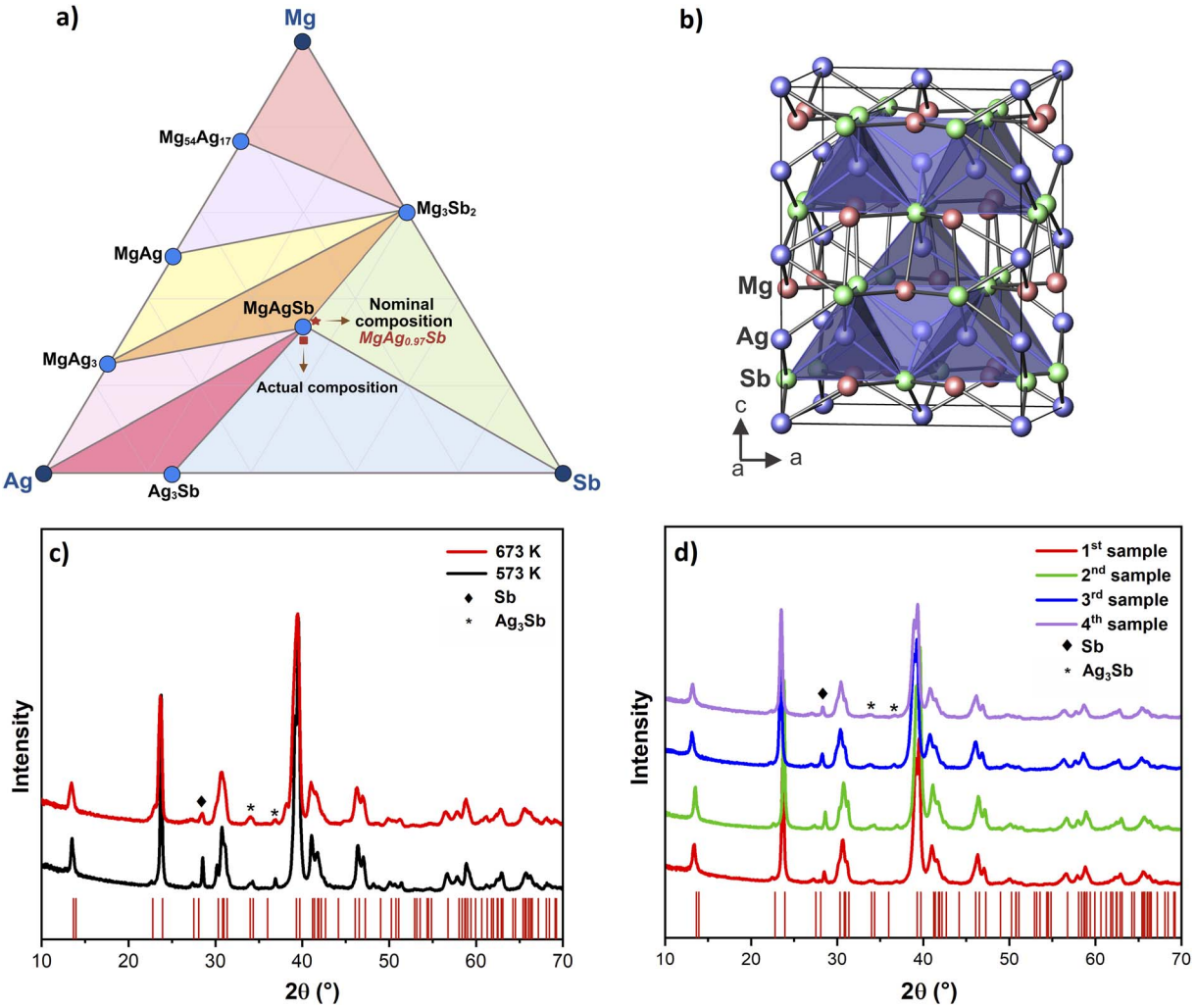

Fig. 2 (a) Isothermal phase diagram of the Mg–Ag–Sb system at 573 K, showing the nominal composition of $MgAg_{0.97}Sb$ (star) and the actual composition (square). (b) Tetragonal crystal structure of α-MgAgSb illustrating the distorted Mg–Sb rocksalt lattice with Ag atoms occupying half of the pseudocubic sites. (c) The XRD patterns of $MgAg_{0.97}Sb$ samples synthesized with different sintering temperatures (573 K or 673 K) and subsequently annealed for 3 d, (d) the XRD patterns of four $MgAg_{0.97}Sb$ samples synthesized using the same method, sintered at 673 K, annealed for 3 d, and subjected to additional heat treatment. The red ticks at the bottom of the XRD patterns indicate the theoretical peak positions of the α phase.

in a LFA 467 light flash apparatus for thermal diffusivity measurements between 323 K and 573 K. C_p was determined using polynomial equation described by Agne *et al.*[56] Sample densities were determined using both the Archimedes method and geometric measurements. Densities above 99% of the theoretical value were achieved for samples sintered at 673 K, while those sintered at 573 K reached approximately 95%, consistent with the literature.[42,45] Bar-shaped samples were used in a ULVAC ZEM-3 system to measure the S and electrical resistivity (ρ), utilizing a four-probe method. Hall-effect measurements were performed using the Van der Pauw technique with a reversible magnetic field of 1 T, employing pressure-assisted tungsten electrodes. n and μ were calculated using the equations $n = \frac{1}{eR_H}$ and $\mu = \sigma R_H$, respectively.

As is commonly reported in the TE literature,[57–59] the typical temperature-averaged experimental uncertainties are approximately ±6% for S, ±8% for ρ, ±11% for κ, and ± 15% for the calculated zT values. For the samples synthesized under different processing conditions, the error bars shown in the relevant figures reflect these standard uncertainty ranges. In contrast, for the set of identically processed $MgAg_{0.97}Sb$ samples (*e.g.*, sintered at 673 K, annealed for 3 days, and subjected to an additional heat treatment), we report reproducibility error bars calculated from the standard deviation of the measured values. This approach provides a more direct and statistically meaningful assessment of the synthesis consistency and reliability of our optimized protocol.

3 Results and discussion

3.1 Phase and crystal structure analysis of MgAgSb

The Mg–Ag–Sb ternary system exhibits a highly complex phase diagram, which significantly complicates the synthesis of phase-pure α-MgAgSb due to the thermodynamic stability of competing phases such as Mg_3Sb_2, Ag_3Sb, and elemental Sb.[60]

In this study, $MgAg_{0.97}Sb$ was chosen as the nominal composition, represented by the star symbol in the green region of Fig. 2a, based on the isothermal Mg–Ag–Sb phase diagram at 573 K. However, XRD and SEM analyses revealed that the actual composition shifted toward the blue region (indicated by the square), likely due to partial Mg loss during processing, caused by evaporation or oxidation. Residing in this region is beneficial as shown by recent work by Duparchy *et al.*,[61] which confirmed that the Ag_3Sb + Sb region is particularly favorable for stabilizing predominantly α-MgAgSb with enhanced TE performance. As reported by Kirkham *et al.*,[26] MgAgSb experiences multiple phase transitions upon heating. Initially, it remains in the low-temperature α phase, which is stable up to 600 K. The tetragonal crystal structure of α-MgAgSb, consisting of a distorted Mg–Sb rocksalt lattice with Ag atoms filling half of the pseudocubic sites, is illustrated in Fig. 2b. As the temperature increases, it transitions into the intermediate β phase before ultimately transforming into the high-temperature γ phase. While α and β phases have a distorted tetragonal structure, the γ phase adopts a cubic half-Heusler structure.[26] In this study, DSC was used to analyze these phase transformations. As shown in Fig. S1, the DSC curve for the best-performing $MgAg_{0.97}Sb$ sample reveals three major endothermic effects: a transition from α-MgAgSb to β-MgAgSb at around 600 K, a second phase transition from β-MgAgSb to γ-MgAgSb near 660 K, and finally, the melting peak of Ag_3Sb impurities at *ca.* 744 K, aligning with previously reported data.[37,62]

To address the issues mentioned above, the α-MgAgSb phase was synthesized using a two-step ball milling method to precisely adjust the composition,[29] followed by extended annealing (3 days) to reduce impurity phases. Among the various synthesis parameters explored, sintering temperature was found to have a significant influence on phase purity. As shown in Fig. 2c, samples sintered at 673 K exhibited significantly improved phase purity compared to those sintered at 573 K. The main diffraction peaks correspond to the α-MgAgSb phase, indexed to the $I\bar{4}c2$ space group, and appear sharper and more well-defined in the 673 K sample. However, minor secondary phases are still present, including a peak at $2\theta = 28.47°$ corresponding to elemental Sb, and peaks at $2\theta = 34°$ and 38.94° attributed to Ag_3Sb. Additionally, samples sintered at 573 K exhibited reproducibility issues, as shown in Fig. S2a, where XRD patterns from samples with the same nominal composition displayed noticeable variations. These discrepancies suggest that sintering at lower temperatures is more sensitive to slight fluctuations in processing conditions, making it less reliable for obtaining $MgAg_{0.97}Sb$ with high purity. The effect of prolonged annealing for 15 days was also evaluated and is presented in Fig. S2b, where further degradation or loss of the α phase was observed. This outcome confirms that sintering at 673 K combined with a 3-days annealing duration offers a more robust and reproducible route for stabilizing the α-MgAgSb phase.

To enhance the reproducibility of sample preparation and minimize discrepancies in electronic transport measurements during heating and cooling cycles, an additional heat treatment step was introduced. This involved heating the sample to 573 K over 4.5 hours, holding the temperature for 10 minutes, and

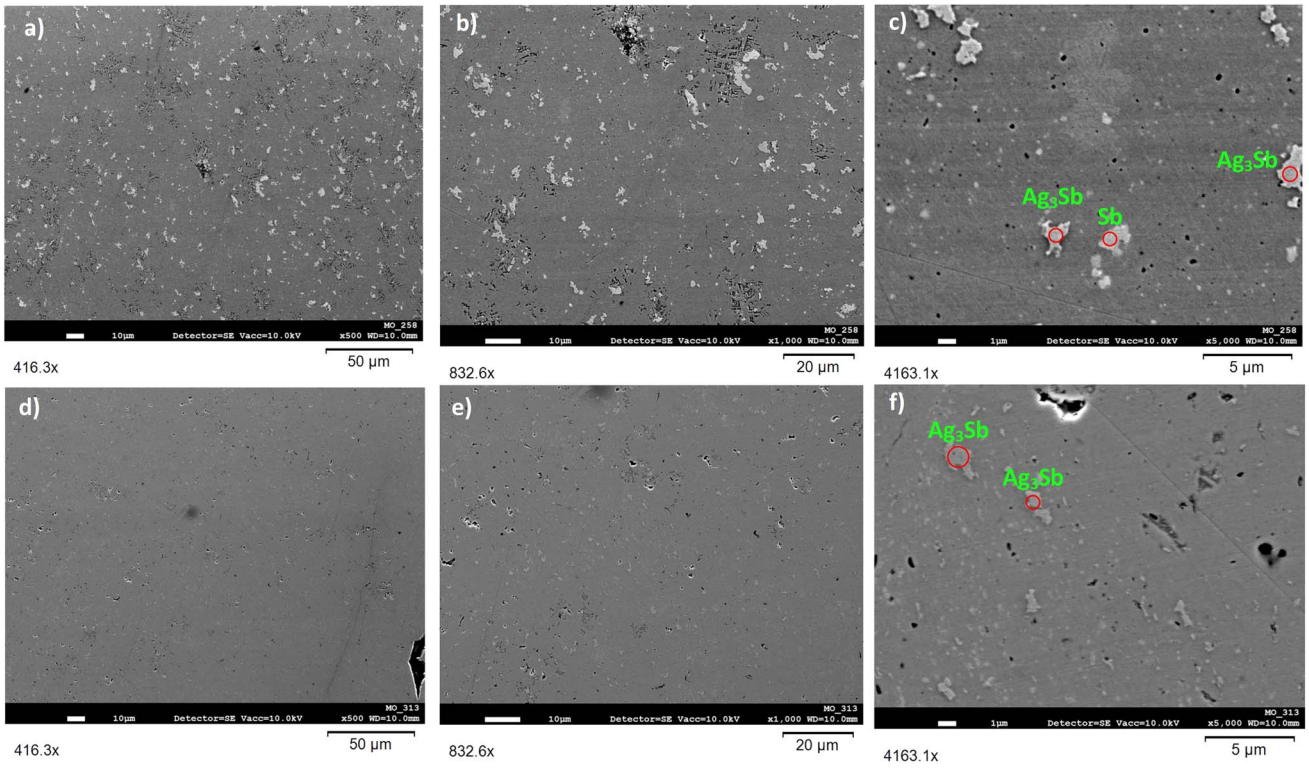

Fig. 3 SEM in secondary electron mode (SE-SEM) images of $MgAg_{0.97}Sb$ samples. (a–c) represent the sample sintered at 573 K and annealed for 3 d; (d–f) show the sample sintered at 673 K and annealed for 3 d.

then allowing it to cool in 3 hours. This adjustment stabilized the material and minimized hysteresis during thermal cycling. Using these refined synthesis methods, α-MgAgSb phase with the composition $MgAg_{0.97}Sb$ was consistently produced, achieving stable and optimized properties. Fig. 2d shows the XRD patterns of four $MgAg_{0.97}Sb$ samples, all synthesized using the improved method. These samples, sintered at 673 K, annealed for 3 days and subjected to additional heat treatment, exhibited enhanced phase stability.

3.2 Microstructure analysis of MgAgSb

Microstructure analysis was performed to better understand the effect of different synthesis conditions. Fig. 3 presents SE-SEM images of $MgAg_{0.97}Sb$ samples. Fig. 3a–c correspond to the sample sintered at 573 K, while Fig. 3d–f represent the sample sintered at 673 K, both with the same 3-days annealing duration. The latter exhibits improved homogeneity and denser packing, consistent with its high relative density (99%), whereas the sample sintered at the lower temperature shows a deviation of approximately 4–5%, indicating a relative density around 94–95%.[42,45,46] In comparison, the sample treated at 673 K with 3-days annealing shows a noticeable reduction in Sb-rich secondary phases, in agreement with the XRD results in Fig. 2c, which display a lower intensity of the Sb-related peak. Nevertheless, the observation of Ag_3Sb-rich and Sb-rich secondary phases is commonly reported in α-MgAgSb.[28,42] As mentioned earlier, although precise compositional control is essential to minimize the formation of secondary phases, being in the Ag_3Sb + Sb-rich region may still be beneficial.[61]

The phase distribution of $MgAg_{0.97}Sb$ sintered at 673 K was further analyzed using energy dispersive X-ray spectroscopy (EDS), as shown in Fig. S3, with the corresponding elemental compositions summarized in Table S1.

3.3 TE transport properties

The transport properties of $MgAg_{0.97}Sb$ samples sintered at 573 K and 673 K with a 3-days annealing duration were evaluated, as shown in Fig. 4 and 5.

As depicted in Fig. 4a, the sample sintered at 673 K exhibits a higher Seebeck coefficient compared to the one processed at the lower temperature. This enhancement is attributed to a reduction in intrinsic defect concentrations, likely governed by retrograde solubility behavior associated with the phase transitions occurring around 600 K and 650 K, as previously discussed. Similar behavior has been reported in TE systems such as PbTe[63] and Bi_2Te_3,[64] where acceptor-type vacancies diminish with increasing temperature. It is therefore plausible that Ag vacancies which identify as the dominant intrinsic defects responsible for hole generation in MgAgSb,[39,65] follow a similar trend with their concentration initially increasing with temperature, as observed in dynamically doped Ag- or Cu-PbTe systems.[66–68] However, at the onset of a phase transition, competing phases may emerge, as seen in Cu_2Se,[69] where the defect concentration may now decrease as temperature is increased, known as "retrograde solubility" of defects. A reduction in Ag vacancy concentration at higher sintering temperatures would thus lower the hole carrier density and result in an enhanced S, even within the same nominal phase composition.

To further understand the variation in electrical transport properties of α-$MgAg_{0.97}Sb$ under different sintering conditions, Hall effect measurements were conducted from room temperature to 523 K to examine n, and μ.

As shown in Fig. 4b, the sample sintered at 673 K exhibits a significantly lower n compared to the one sintered at 573 K. This finding aligns with the retrograde solubility discussion, suggesting that higher sintering temperatures reduce the concentration of Ag vacancies. Samples sintered at 673 K display higher resistivity, as seen in Fig. 4c, which can be primarily attributed to their lower carrier concentration rather than differences in charge transport mechanisms.

As shown in Fig. 4d, PF is notably enhanced for the sample sintered at 673 K, reaching 16.04 μW cm^{-1} K^{-2} at low temperatures. This represents an improvement of approximately 19% compared to the sample sintered at 573 K, which exhibits a PF of 13.43 μW cm^{-1} K^{-2}. This enhanced PF directly contributes to improved electronic transport behavior.

μ_w, a key parameter influencing TE performance, was calculated to better understand the origin of the high PF observed in α-$MgAg_{0.97}Sb$ samples sintered at a higher temperature. As described in eqn (1), μ_w was evaluated based on the measured S and σ using the following relation:[70]

$$\mu_w = \frac{3h^3\sigma}{8\pi e(2m_e k_B T)^{3/2}} \left(\frac{\exp\left(\frac{|S|}{k_B/e} - 2\right)}{1+\exp\left(-5\left(\frac{|S|}{k_B/e} - 1\right)\right)} + \frac{\frac{3}{\pi^2}\frac{|S|}{k_B/e}}{1+\exp\left(5\left(\frac{|S|}{k_B/e} - 1\right)\right)} \right) \quad (1)$$

The temperature-dependent μ_w of $MgAg_{0.97}Sb$ samples, as illustrated in Fig. 4e, varies significantly with sintering temperature. The sample sintered at 673 K exhibits the highest μ_w, reaching approximately 180 cm^2 V^{-1} s^{-1} at 323 K, which is indicative of enhanced charge transport.

As depicted in Fig. 4f, μ also increases substantially with sintering temperature. The sample sintered at 673 K reaches a μ of approximately 110 cm^2 V^{-1} s^{-1}at room temperature, which is about 53% higher than that of the 573 K sample (72 cm^2 V^{-1} s^{-1}), consistent with the trend observed in μ_w.

κ is presented in Fig. 5a and shows no significant difference between the samples sintered at 573 K and 673 K across the measured temperature range. To gain further insights into the thermal transport mechanisms, κ was deconvoluted into its electronic (κ_e) and lattice (κ_l) components, where $\kappa = \kappa_e + \kappa_l$. κ_e was calculated using the Wiedemann–Franz law, as shown in eqn (2), with L representing the Lorenz number and σ.[71]

$$\kappa_e = L\sigma T \quad (2)$$

As illustrated in Fig. 5b, κ_e increases with temperature due to the rise in σ. The κ_l, derived by subtracting κ_e from κ, is

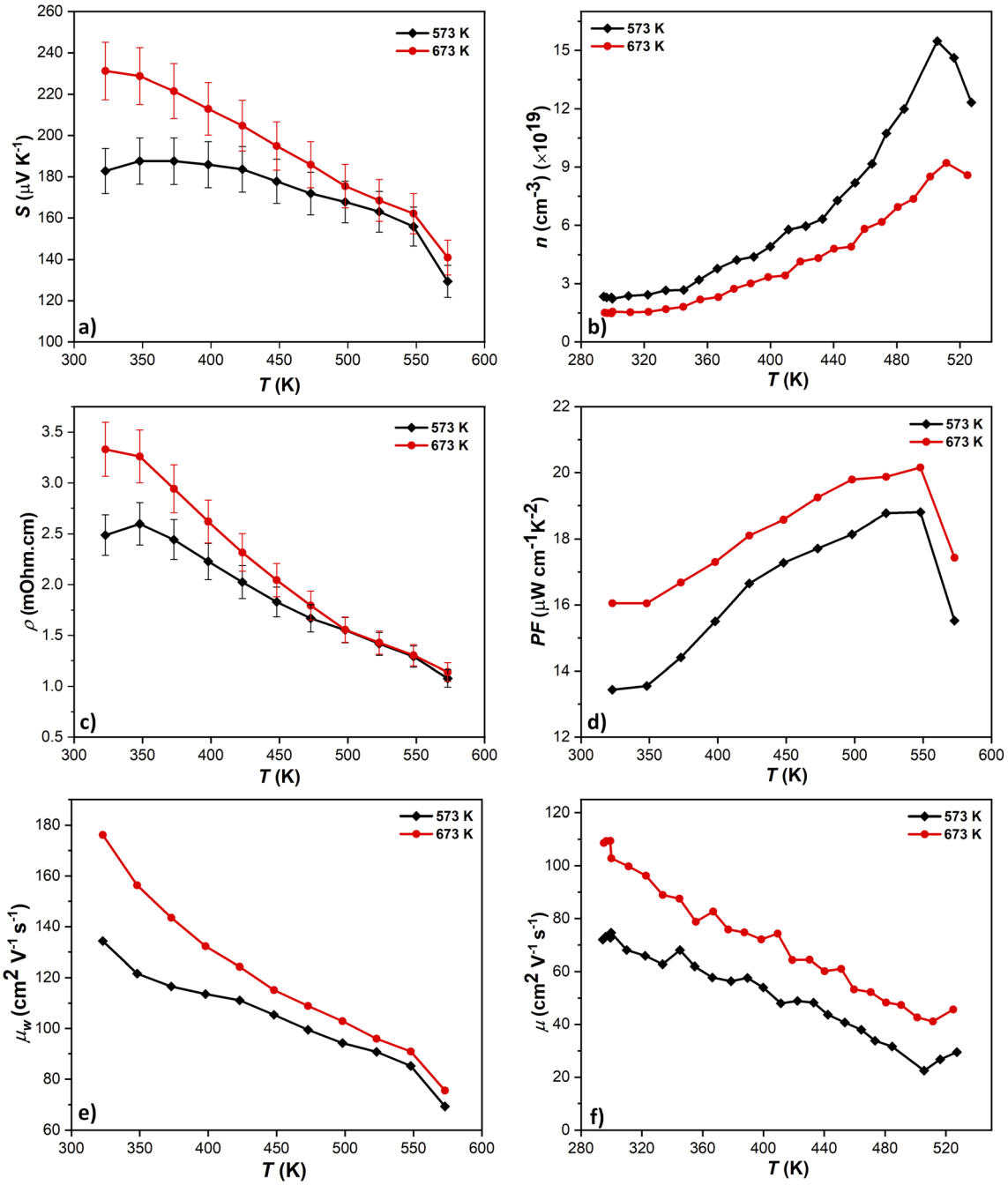

Fig. 4 Temperature-dependent TE transport properties (heating data) of $MgAg_{0.97}Sb$ samples synthesized under different sintering conditions (573 K or 673 K) and annealed for 3 d. (a) Seebeck coefficient (S), (b) carrier concentration (n), (c) electrical resistivity (ρ), (d) power factor ($S^2\sigma$), (e) weighted mobility (μ_w), and (f) Hall mobility (μ). Error bars indicate the measurement uncertainties, taken as 6% for S, 8% for ρ.

presented in Fig. 5c. The sample sintered at 673 K exhibits slightly higher κ_l values, suggesting reduced phonon scattering, possibly due to decreased porosity. Regarding TE performance (Fig. 5d), the highest zT value of 0.6 was observed at 323 K for the sample sintered at 673 K, compared to 0.51 for the other sample. Although these variations fall within the typical experimental error range, an additional concern with sintering at 573 K is the lack of reproducibility, as samples with the same nominal composition exhibited noticeable variations in transport properties, as demonstrated in Fig. S4.

This result demonstrates that increasing the sintering temperature effectively enhances material performance by achieving a favorable balance between electronic and thermal transport properties. Furthermore, the effect of prolonged annealing for 15 days was further investigated, and the detailed results are provided in Fig. S5, which confirm that a 3-days annealing duration is more favorable for achieving optimal TE performance.

Although the samples sintered at 673 K exhibited the highest TE performance, the measurements revealed noticeable

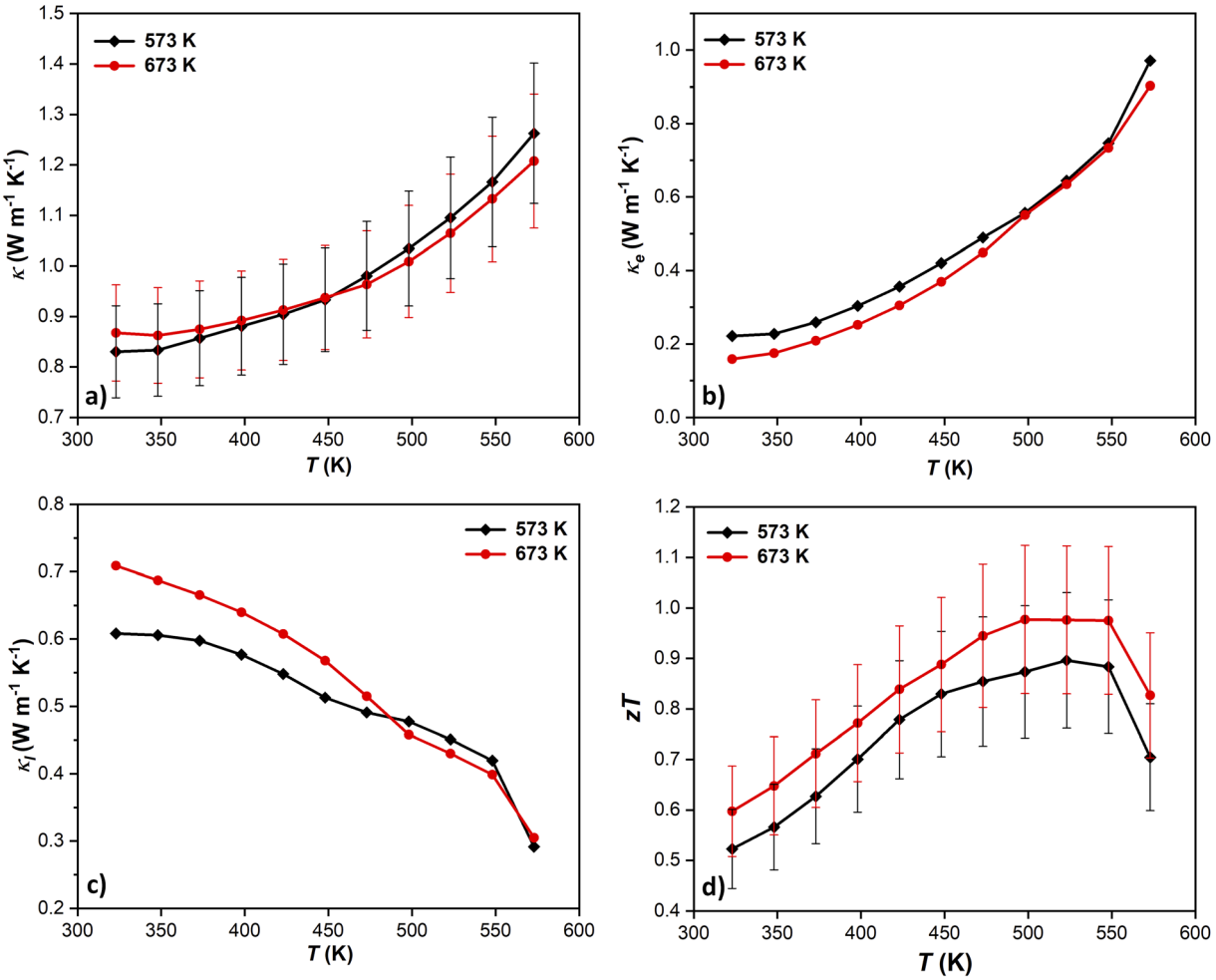

Fig. 5 Temperature-dependent TE transport properties (heating data) of $MgAg_{0.97}Sb$ samples synthesized under different sintering conditions (573 K or 673 K) and annealed for 3 d. (a) Total thermal conductivity (κ), (b) electronic thermal conductivity (κ_e), (c) lattice thermal conductivity (κ_l), (d) zT. Error bars indicate the measurement uncertainties, taken as 11% for κ, and 15% for zT.

hysteresis between heating and cooling cycles, particularly in the ρ as shown in Fig. S6b. This hysteresis influenced the zT values, with the cooling curve displaying a significantly higher zT at low temperatures, increasing from 0.6 to 0.73 around 323 K as seen in Fig. S6d.

To address this, an additional heat treatment step was applied to $MgAg_{0.97}Sb$ samples sintered at 673 K and annealed for 3 days, as shown in the synthesis schematic (Fig. 1b). This process involved heating the sample to 573 K over 4.5 hours, maintaining it at that temperature for 10 minutes, and then gradually cooling it to room temperature over 3 hours. The electronic transport properties of the heat-treated samples, shown in Fig. 6, confirm that this approach successfully eliminates hysteresis and enhances reproducibility. The electronic and thermal transport data (Fig. 6a–f) show consistent results within the experimental error for multiple synthesized samples. As Fig. 6f highlights, these optimizations result in consistently high zT values, reaching 0.84 near room temperature and 1.3 at 500 K. The error bars in these figures were calculated from the standard deviation of measurements across four identically processed samples, directly reflecting the reproducibility of our synthesis approach. Notably, all error bars are smaller than the typical experimental uncertainties commonly reported in the TE literature (±6% for S, ±8% for ρ, ±11% for κ, and ±15% for zT),[57–59] yet remain within acceptable bounds, thereby confirming the reliability and consistency of our measurements.

As summarized in Table S2, the zT values achieved in this work exceed those reported in many prior studies and closely approach the highest values in the literature, most of which required chemical doping for performance enhancement.[26,28,29,40,43–47,50,72,73] Importantly, our undoped samples deliver this level of performance with reproducibility, representing a significant advancement toward a reliable and scalable synthesis protocol for α-MgAgSb.

To evaluate the potential irreversibility of the best-performing $MgAg_{0.97}Sb$ samples, we conducted XRD and SEM analyses after heating–cooling cycles (Fig. S7). The XRD results confirm that the crystal structure remains intact, with no signs of further phase decomposition or secondary phase formation. Similarly, SEM images of the 1st and 4th samples before and after cycling show no significant microstructural changes,

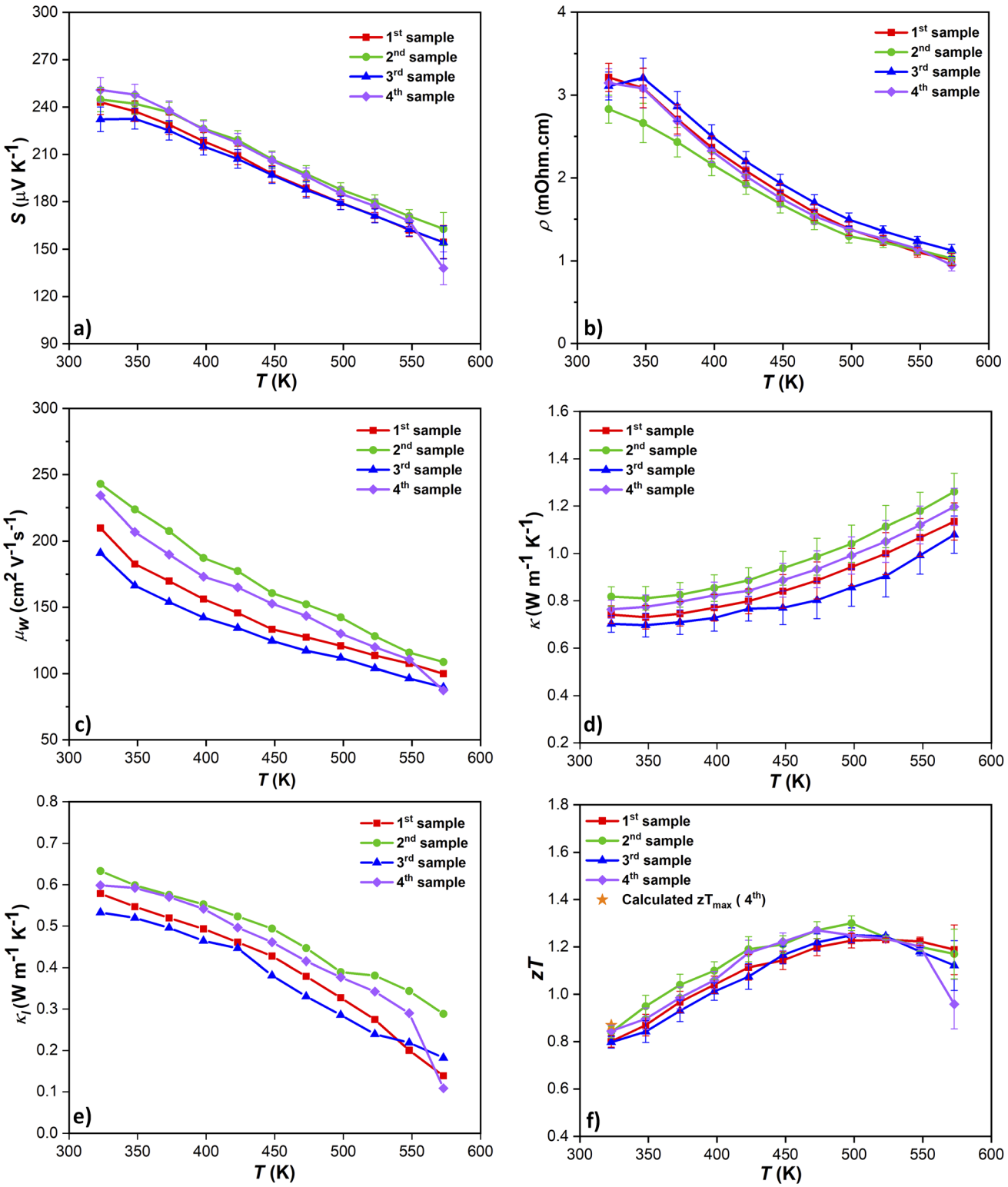

Fig. 6 Temperature-dependent TE transport properties of four $MgAg_{0.97}Sb$ samples synthesized under the same conditions (sintered at 673 K, annealed for 3 d, followed by additional heat treatment). (a) Seebeck coefficient (S), (b) electrical resistivity (ρ), (c) weighted mobility (μ_w), (d) total thermal conductivity (κ), (e) lattice thermal conductivity (κ_l), and (f) zT. Error bars represent the standard deviations calculated from the four samples.

indicating that no major morphological degradation occurred during thermal cycling.

Further investigation was carried out to determine when the best performing samples show stable transport properties. To address this, two consecutive cycles of heating and cooling were performed using ZEM-3 and LFA measurements to assess resistivity, S, and κ, respectively. The measurements were conducted on the 4th sample (sintered at 673 K, annealed for 3

days, followed by additional heat treatment), and the confirming results are presented in Fig. S8.

As shown in Fig. 7, the room temperature μ_w was calculated using the measured S and σ across five samples synthesized under different conditions. The sample sintered at 673 K for 3 days exhibited a significantly higher μ_w of approximately 176 $cm^2\ V^{-1}\ s^{-1}$, compared to 134 $cm^2\ V^{-1}\ s^{-1}$ for the 573 K counterpart. The highest μ_w value, 234 $cm^2\ V^{-1}\ s^{-1}$, was achieved after a second annealing step, suggesting enhanced charge transport likely due to improved phase purity and reduced carrier scattering. This improvement is primarily attributed to the gradual removal of Ag_3Sb impurities, which are known to act as scattering centers. As demonstrated by Tan *et al.*,[49] Ag d-orbitals contribute significantly to two of the three valence band maxima in MgAgSb. Therefore, while the removal of Ag-based secondary phases such as Ag_3Sb is beneficial for transport, preserving adequate Ag content within the primary phase is essential to maintain valence band convergence and sustain high μ_w.

In addition to the enhanced μ_w, B-factor was calculated using eqn (3), which incorporates μ_w and κ_l.[5,74]

$$B = \frac{8\pi k_B (2m_e)^{3/2}}{3eh^3}(k_B T)^{5/2} \cdot \frac{\mu_w}{\kappa_l} \quad (3)$$

As shown in Fig. 7, the sample sintered at high temperature and subjected to a second annealing step exhibited a significantly higher B at 323 K compared to the other samples. The primary advantage of calculating B is its ability to assess whether the n is near optimal. In this case, the excellent agreement between the calculated and measured zT_{max} strongly supports that conclusion. Using $B = 0.317$, the maximum theoretical zT at low temperatures was calculated for the 4th sample, yielding a value of approximately 0.87 at 323 K, as indicated by the star marker in Fig. 6f. This close match with the experimental result confirms that the sample exhibits near-optimal performance.

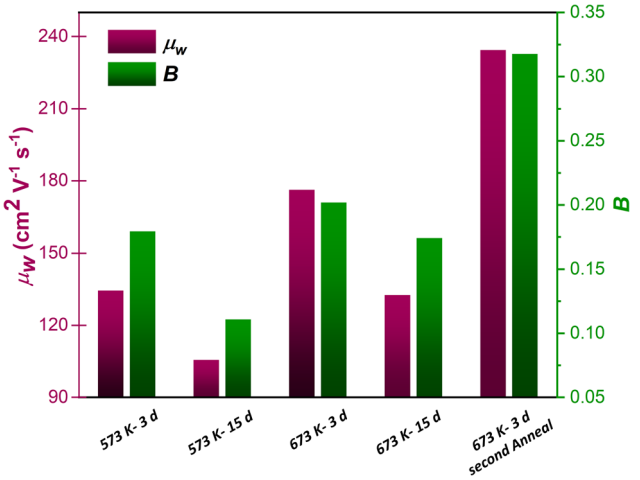

Fig. 7 Comparison of weighted mobility (μ_w) and electronic quality factor (B) at 323 K for α-$MgAg_{0.97}Sb$ samples synthesized using different methods.

Fig. 8a presents the temperature-dependent n and μ of best performing samples. Compared to other studies, our sample shows a lower carrier concentration, approximately 1.8×10^{19} cm^{-3} at low temperatures.[72,75–77] In contrast, μ is relatively high, reaching around 130 $cm^2\ cm^2\ V^{-1}\ s^{-1}$ near room temperature, which is significantly higher than values reported in other works, such as 76 $cm^2\ V^{-1}s^{-1}$ [42,44], 58 $cm^2\ V^{-1}s^{-1}$ [76], and 50 $cm^2\ V^{-1}s^{-1}$ [41] at room temperature.

Fig. 8b shows the temperature-dependent carrier concentration, which does not change after multiple cycles. To further assess the reproducibility of our results, Fig. S9 present n and μ, respectively, for two samples prepared identically using the developed method with the same $MgAg_{0.97}Sb$ composition. This graph demonstrates consistent trends in both n and μ across the two samples, thereby confirming the reproducibility of the high-performing α-$MgAg_{0.97}Sb$. The close alignment of the data points between the samples indicates that our synthesis and preparation methods reliably produce materials with uniform electronic transport properties.

3.4 Mechanical properties of MgAgSb

Mechanical robustness is essential for the manufacturing, assembly, and reliable operation of TE devices, as they often function under cyclic temperature gradients, where inadequate strength can compromise reliability and degrade performance under thermal stress.[78] The mechanical properties of nanostructured α-MgAgSb are known to be superior compared to other promising p-type TE materials that function in the low to medium temperature range.[65–67,79] DFT simulations further support this by reporting an ideal shear strength of 3.25 GPa for α-MgAgSb, indicating good intrinsic mechanical stability under shear loading.[30] As previously mentioned, hardness measurements were performed at eight different points on the sample, and the average of these values was used to determine the material's hardness. The $MgAg_{0.97}Sb$ sample exhibiting the highest performance exhibited an average hardness of 302.5 HV (2.97 GPa). One representative measurement, shown in Fig. 9a, recorded a hardness of 302 HV (2.96 GPa) in a specific region. Since hardness measurements can be influenced by the applied load, a higher load generally enhances accuracy and reliability.[80] Therefore, a maximum load of approximately 2.942 N with a 10-seconds holding time was applied, which exceeds the loads used in previous studies.[81,82] Notably, when compared to other low-to mid-temperature p-type TE materials as shown in the bar graph of Fig. 9b, the hardness of $MgAg_{0.97}Sb$ is significantly higher than those of p-type $Bi_{0.5}Sb_{1.5}Te_3$ (0.64 GPa),[83] Ge-doped PbTe (2.3 GPa),[84] Na-doped PbSe (0.62 GPa),[85] $Cu_{1.8}S$-1% Ru bulk composites (1.22 GPa),[86] and $Cu_3Sb_{0.93}Co_{0.04}Sn_{0.03}Se_4$ (1.29 GPa).[9] Although slightly lower than the hardness of ZnSb[87] and p-type skutterudite $Mm_{0.9}Fe_{3.1}Co_{0.9}Sb_{12}$,[88] the hardness of $MgAg_{0.97}Sb$ remains in a favorable range that ensures good mechanical robustness without compromising TE performance or integration reliability. Additionally, while high hardness can sometimes be associated with increased κ or brittleness, this does not appear to be the case here.

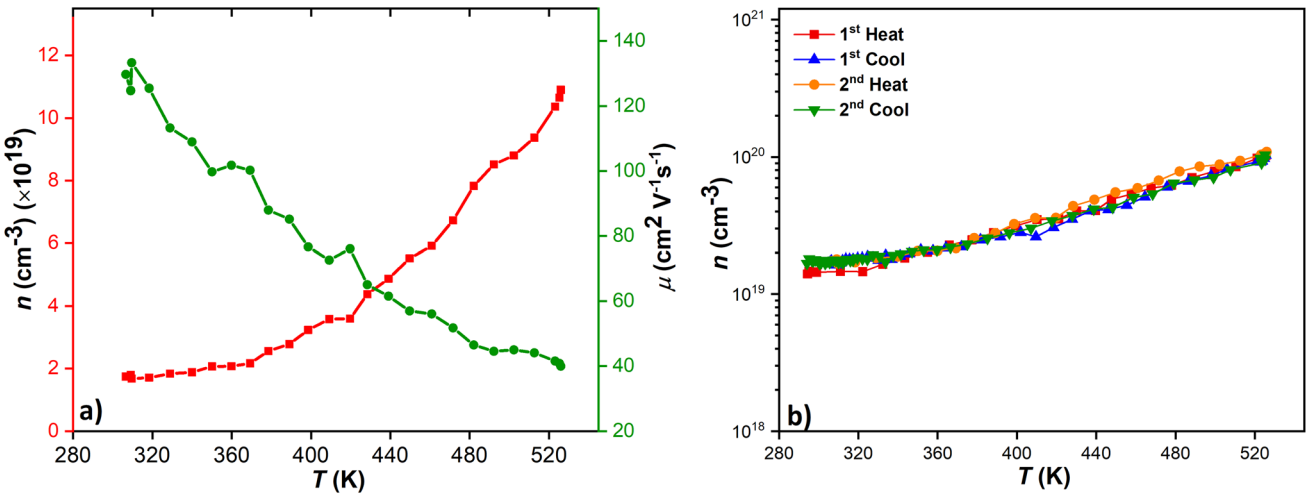

Fig. 8 Hall effect measurements of α-$MgAg_{0.97}Sb$ for the sample sintered at 673 K, annealed for 3 d, followed by additional heat treatment. (a) Temperature dependence of carrier concentration (n) and Hall mobility (μ) for the sample sintered at 673 K and (b) n across two complete cycles of temperature variation of same sample.

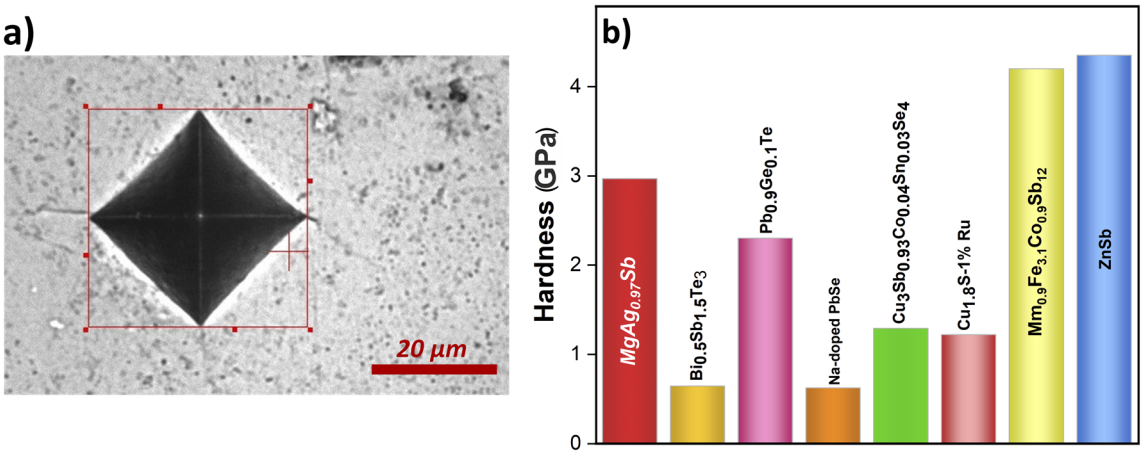

Fig. 9 (a) Vickers hardness measurements of the best-performing $MgAg_{0.97}Sb$ sample (sintered at 673 K, annealed for 3 d, followed by additional heat treatment), showing an indent with a measured value of 302 HV. (b) Comparison of the hardness of $MgAg_{0.97}Sb$ with various p-type TE materials, highlighting its superior mechanical strength relative to commonly studied compounds.

4 Conclusion

In this study, we systematically explored various synthesis strategies to reproducibly fabricate α-MgAgSb TE materials and identified optimal processing conditions. The best TE performance was achieved by sintering $MgAg_{0.97}Sb$ samples at 673 K, followed by a 3-days annealing period and an additional low-temperature stabilization step. These optimized conditions resulted in consistent, enhanced performance, achieving a peak zT of approximately 0.84 near room temperature and reaching values as high as 1.3 at 500 K. A primary contributor to this outstanding performance was the notably high μ (~130 $cm^2 V^{-1} s^{-1}$ at room temperature), indicative of improved electronic transport properties. SEM analysis revealed that the optimized samples possessed a somewhat heterogeneous microstructure, while mechanical testing confirmed hardness values on par with previously reported results. Importantly, XRD and SEM analyses after thermal cycling confirmed the structural and morphological stability of the optimized samples, further supporting their practical viability. Overall, our findings establish α-MgAgSb as a promising, reproducible, and scalable candidate for sustainable, low-temperature TE applications, free of toxic or scarce elements.

Author contributions

Saba Sepahban Shahgoli: data curation, formal analysis, investigation, methodology, writing – original draft, writing – review & editing. Melis Ozen: data curation, formal analysis, investigation, methodology, writing – original draft, writing – review & editing. Duncan Zavanelli: formal analysis, investigation, writing – original draft, writing – review & editing. Gulchin

Aliyeva: formal analysis, investigation, writing – original draft. Arda Baran Burcak: formal analysis, investigation, writing – original draft. Ulrich Burkhardt: formal analysis, investigation, writing – original draft. Eleonora Isotta: formal analysis, investigation, writing – original draft, writing – review & editing. G. Jeffrey Snyder: supervision, formal analysis, writing – review & editing. Umut Aydemir: conceptualization, investigation, resources, supervision, funding acquisition, writing – review & editing.

Conflicts of interest

The authors declare no competing financial interest.

Data availability

The Supporting Information includes comprehensive data and analyses on DSC measurements, XRD patterns, EDS composition analysis, TE transport properties, and Hall effect data evaluations. See DOI: **https://doi.org/10.1039/d5ta05284j**.

Acknowledgements

U. A. acknowledges TÜBİTAK for financial support through project number 223M182. M. O. acknowledges financial support from Turkish Aerospace (TUSAŞ) under project number TM4111 and from the Scientific and Technological Research Council of Türkiye (TÜBİTAK) under project numbers 20AG001 and 20AG020. D. Z. was supported by a NASA Space Technology Graduate Research Opportunity. We also thank Barış Yağcı and the team at the Koç University Surface Science and Technology Center (KUYTAM) for their assistance with SEM measurements.

References

1 G. Schierning, Bring on the Heat, *Nat. Energy*, 2018, **3**(2), 92–93, DOI: **10.1038/s41560-018-0093-4**.
2 R. A. Kishore and S. Priya, A Review on Low-Grade Thermal Energy Harvesting: Materials, Methods and Devices, *Materials*, 2018, DOI: **10.3390/ma11081433**.
3 X. Shi and J. He, Thermopower and Harvesting Heat, *Science*, 2021, **371**(6527), 343–344, DOI: **10.1126/science.abf3342**.
4 X. L. Shi, J. Zou and Z. G. Chen, Advanced Thermoelectric Design: From Materials and Structures to Devices, *Chem. Rev.*, 2020, **120**(15), 7399–7515, DOI: **10.1021/acs.chemrev.0c00026**.
5 G. J. Snyder and E. S. Toberer, Complex Thermoelectric Materials, *Nat. Mater.*, 2008, **7**(2), 105–114, DOI: **10.1038/nmat2090**.
6 D. Zhao and G. Tan, A Review of Thermoelectric Cooling: Materials, Modeling and Applications, *Appl. Therm. Eng.*, 2014, **66**(1), 15–24, DOI: **10.1016/j.applthermaleng.2014.01.074**.
7 D. M. Rowe, *CRC Handbook of Thermoelectrics*, CRC Press, Boca Raton, FL, 1995.
8 R. Freer, D. Ekren, T. Ghosh, K. Biswas, P. Qiu, S. Wan, L. Chen, S. Han, C. Fu, T. Zhu, A. K. M. Ashiquzzaman Shawon, A. Zevalkink, K. Imasato, G. J. Snyder, M. Ozen, K. Saglik, U. Aydemir, R. Cardoso-Gil, E. Svanidze, R. Funahashi, A. V. Powell, S. Mukherjee, S. Tippireddy, P. Vaqueiro, F. Gascoin, T. Kyratsi, P. Sauerschnig and T. Mori, Key Properties of Inorganic Thermoelectric Materials—Tables (Version 1), *J. Phys.: Energy*, 2022, **4**(2), 22002, DOI: **10.1088/2515-7655/ac49dc**.
9 S. Wei, L. Yu, Z. Ji, S. Luo, J. Liang, T. Wang, W. Song and S. Zheng, Enhancing the Thermoelectric and Mechanical Properties of Cu3SbSe4-Based Materials by Defect Engineering and Covalent Bonds Reinforcement, *J. Alloys Compd.*, 2024, **997**, 174961, DOI: **10.1016/j.jallcom.2024.174961**.
10 K. Saglik, M. Yahyaoglu, C. Candolfi and U. Aydemir, Enhancing Thermoelectric and Mechanical Properties of P-Type (Bi, Sb)$_2$Te$_3$ through Rickardite Mineral (Cu$_2$.9Te$_2$) Incorporation, *Chem. Mater.*, 2023, **35**(9), 3603–3613, DOI: **10.1021/acs.chemmater.3c00229**.
11 H. Li, X. Su, X. Tang, Q. Zhang, C. Uher, G. J. Snyder and U. Aydemir, Grain Boundary Engineering with Nano-Scale InSb Producing High Performance InxCeyCo4Sb12 + z Skutterudite Thermoelectrics, *J. Mater.*, 2017, **3**(4), 273–279, DOI: **10.1016/j.jmat.2017.07.003**.
12 X. Shi, J. Yang, J. R. Salvador, M. Chi, J. Y. Cho, H. Wang, S. Bai, J. Yang, W. Zhang and L. Chen, Multiple-Filled Skutterudites: High Thermoelectric Figure of Merit through Separately Optimizing Electrical and Thermal Transports, *J. Am. Chem. Soc.*, 2011, **133**(20), 7837–7846, DOI: **10.1021/ja111199y**.
13 O. Delaire, J. Ma, K. Marty, a F. May, M. a McGuire, M.-H. Du, D. J. Singh, A. Podlesnyak, G. Ehlers, M. D. Lumsden and B. C. Sales, Giant Anharmonic Phonon Scattering in PbTe, *Nat. Mater.*, 2011, **10**(8), 614–619, DOI: **10.1038/nmat3035**.
14 H. Xie, H. Wang, Y. Pei, C. Fu, X. Liu, G. J. Snyder, X. Zhao and T. Zhu, Beneficial Contribution of Alloy Disorder to Electron and Phonon Transport in Half-Heusler Thermoelectric Materials, *Adv. Funct. Mater.*, 2013, **23**(41), 5123–5130, DOI: **10.1002/adfm.201300663**.
15 S. Ohno, U. Aydemir, M. Amsler, J.-H. Pöhls, S. Chanakian, A. Zevalkink, M. A. White, S. K. Bux, C. Wolverton and G. J. Snyder, Achieving ZT > 1 in Inexpensive Zintl Phase Ca9Zn4+Sb9 by Phase Boundary Mapping, *Adv. Funct. Mater.*, 2017, **27**(20), 1606361, DOI: **10.1002/adfm.201606361**.
16 S. R. Brown, S. M. Kauzlarich, F. Gascoin and G. J. Snyder, Yb$_{14}$MnSb$_{11}$: New High Efficiency Thermoelectric Material for Power Generation, *Chem. Mater.*, 2006, **18**(7), 1873–1877, DOI: **10.1021/cm060261t**.
17 B. Yu, M. Zebarjadi, H. Wang, K. Lukas, H. Wang, D. Wang, C. Opeil, M. Dresselhaus, G. Chen and Z. Ren, Enhancement of Thermoelectric Properties by Modulation-Doping in Silicon Germanium Alloy Nanocomposites, *Nano Lett.*, 2012, **12**(4), 2077–2082, DOI: **10.1021/nl3003045**.
18 L.-D. Zhao, S.-H. Lo, Y. Zhang, H. Sun, G. Tan, C. Uher, C. Wolverton, V. P. Dravid and M. G. Kanatzidis, Ultralow Thermal Conductivity and High Thermoelectric Figure of

Merit in SnSe Crystals, *Nature*, 2014, **508**(7496), 373–377, DOI: 10.1038/nature13184.

19 H. Han, L. Zhao, X. Wu, B. Zuo, S. Bian, T. Li, X. Liu, Y. Jiang, C. Chen, J. Bi, J. Xu and L. Yu, Advancements in Thermoelectric Materials: Optimization Strategies for Enhancing Energy Conversion, *J. Mater. Chem. A*, 2024, 24041–24083, DOI: 10.1039/d4ta03666b.

20 B. Poudel, Q. Hao, Y. Ma, Y. Lan, A. Minnich, B. Yu, X. Yan, D. Wang, A. Muto, D. Vashaee, X. Chen, J. Liu, M. S. Dresselhaus, G. Chen and Z. Ren, High-Thermoelectric Performance of Nanostructured Bismuth Antimony Telluride Bulk Alloys, *Science*, 2008, **320**(5876), 634–638, DOI: 10.1126/science.1156446.

21 F. Hao, P. Qiu, Y. Tang, S. Bai, T. Xing, H.-S. Chu, Q. Zhang, P. Lu, T. Zhang, D. Ren, J. Chen, X. Shi and L. Chen, High Efficiency Bi $_2$ Te $_3$ -Based Materials and Devices for Thermoelectric Power Generation between 100 and 300 °C, *Energy Environ. Sci.*, 2016, **9**(10), 3120–3127, DOI: 10.1039/C6EE02017H.

22 X. Hu, K. Nagase, P. Jood, M. Ohta and A. Yamamoto, Power Generation Evaluated on a Bismuth Telluride Unicouple Module, *J. Electron. Mater.*, 2015, **44**(6), 1785–1790, DOI: 10.1007/s11664-014-3556-9.

23 J. Mao, H. Zhu, Z. Ding, Z. Liu, G. A. Gamage, G. Chen and Z. Ren, High Thermoelectric Cooling Performance of N-Type Mg $_3$ Bi $_2$ -Based Materials, *Science*, 2019, **365**(6452), 495–498, DOI: 10.1126/science.aax7792.

24 J. Mao, Y. Wu, S. Song, J. Shuai, Z. Liu, Y. Pei and Z. Ren, Anomalous Electrical Conductivity of N-Type Te-Doped Mg3.2Sb1.5Bi0.5, *Mater. Today Phys.*, 2017, **3**, 1–6, DOI: 10.1016/j.mtphys.2017.08.001.

25 M. Wood, J. J. Kuo, K. Imasato and G. J. Snyder, Improvement of Low-Temperature ZT in a Mg3Sb2–Mg3Bi2 Solid Solution via Mg-Vapor Annealing, *Adv. Mater.*, 2019, **31**(35), 1902337, DOI: 10.1002/adma.201902337.

26 M. J. Kirkham, A. M. dos Santos, C. J. Rawn, E. Lara-Curzio, J. W. Sharp and A. J. Thompson, Ab Initio Determination of Crystal Structures of the Thermoelectric Material MgAgSb, *Phys. Rev. B*, 2012, **85**(14), 144120, DOI: 10.1103/PhysRevB.85.144120.

27 Z. Liu, W. Gao, X. Meng, X. Li, J. Mao, Y. Wang, J. Shuai, W. Cai, Z. Ren and J. Sui, Mechanical Properties of Nanostructured Thermoelectric Materials α-MgAgSb, *Scr. Mater.*, 2017, **127**, 72–75, DOI: 10.1016/j.scriptamat.2016.08.037.

28 P. Ying, X. Liu, C. Fu, X. Yue, H. Xie, X. Zhao, W. Zhang and T. Zhu, High Performance α-MgAgSb Thermoelectric Materials for Low Temperature Power Generation, *Chem. Mater.*, 2015, **27**(3), 909–913, DOI: 10.1021/cm5041826.

29 H. Zhao, J. Sui, Z. Tang, Y. Lan, Q. Jie, D. Kraemer, K. McEnaney, A. Guloy, G. Chen and Z. Ren, High Thermoelectric Performance of MgAgSb-Based Materials, *Nano Energy*, 2014, **7**, 97–103, DOI: 10.1016/j.nanoen.2014.04.012.

30 G. Li, Q. An, U. Aydemir, S. I. Morozov, B. Duan, P. Zhai, Q. Zhang and W. A. Goddard, Intrinsic Mechanical Behavior of MgAgSb Thermoelectric Material: An Ab Initio Study, *J. Mater.*, 2020, **6**(1), 24–32, DOI: 10.1016/j.jmat.2019.11.002.

31 H. Tamaki, H. K. Sato and T. Kanno, Isotropic Conduction Network and Defect Chemistry in Mg3+Sb2-Based Layered Zintl Compounds with High Thermoelectric Performance, *Adv. Mater.*, 2016, **28**(46), 10182–10187, DOI: 10.1002/adma.201603955.

32 Z. Liu, W. Gao, H. Oshima, K. Nagase, C.-H. Lee and T. Mori, Maximizing the Performance of N-Type Mg3Bi2 Based Materials for Room-Temperature Power Generation and Thermoelectric Cooling, *Nat. Commun.*, 2022, **13**(1), 1120, DOI: 10.1038/s41467-022-28798-4.

33 M. Ozen, M. Yahyaoglu, C. Candolfi, I. Veremchuk, F. Kaiser, U. Burkhardt, G. J. Snyder, Y. Grin and U. Aydemir, Enhanced Thermoelectric Performance in Mg_3+xSb1.5Bi0.49Te0.01via Engineering Microstructure through Melt-Centrifugation, *J. Mater. Chem. A*, 2021, **9**(3), 1733–1742, DOI: 10.1039/D0TA09993G.

34 Z. Liu, N. Sato, W. Gao, K. Yubuta, N. Kawamoto, M. Mitome, K. Kurashima, Y. Owada, K. Nagase, C.-H. Lee, J. Yi, K. Tsuchiya and T. Mori, Demonstration of Ultrahigh Thermoelectric Efficiency of ∼7.3% in Mg3Sb2/MgAgSb Module for Low-Temperature Energy Harvesting, *Joule*, 2021, **5**(5), 1196–1208, DOI: 10.1016/j.joule.2021.03.017.

35 K. Imasato, M. Wood, S. Anand, J. J. Kuo and G. J. Snyder, Understanding the High Thermoelectric Performance of Mg3Sb2-Mg3Bi2 Alloys, *Adv. Energy Sustainability Res.*, 2022, **3**(6), 2100208, DOI: 10.1002/aesr.202100208.

36 M. Ozen, A. B. Burcak, D. Zavanelli, M. Heo, M. Yahyaoglu, Y. Oz, U. Burkhardt, H.-S. Kim, G. J. Snyder and U. Aydemir, Realizing Ultrahigh Near-Room-Temperature Thermoelectric Figure of Merit for N-Type $Mg_3(Sb,Bi)_2$ through Grain Boundary Complexion Engineering with Niobium, *ACS Appl. Mater. Interfaces*, 2024, **16**(39), 52501–52514, DOI: 10.1021/acsami.4c12046.

37 A. Li, C. Fu, X. Zhao and T. Zhu, High-Performance Mg3Sb2-XBix Thermoelectrics: Progress and Perspective, *Research*, 2020, DOI: 10.34133/2020/1934848.

38 T. Kanno, H. Tamaki, H. K. Sato, S. D. Kang, S. Ohno, K. Imasato, J. J. Kuo, G. J. Snyder and Y. Miyazaki, Enhancement of Average Thermoelectric Figure of Merit by Increasing the Grain-Size of Mg3.2Sb1.5Bi0.49Te0.01, *Appl. Phys. Lett.*, 2018, **112**(3), 33903, DOI: 10.1063/1.5016488.

39 Z. Liu, J. Mao, J. Sui and Z. Ren, High Thermoelectric Performance of α-MgAgSb for Power Generation, *Energy Environ. Sci.*, 2018, **11**(1), 23–44, DOI: 10.1039/C7EE02504A.

40 Y. Zheng, C. Liu, L. Miao, H. Lin, J. Gao, X. Wang, J. Chen, S. Wu, X. Li and H. Cai, Cost Effective Synthesis of P-Type Zn-Doped MgAgSb by Planetary Ball-Milling with Enhanced Thermoelectric Properties, *RSC Adv.*, 2018, **8**(62), 35353–35359, DOI: 10.1039/C8RA06765A.

41 Y. Zheng, C. Liu, L. Miao, C. Li, R. Huang, J. Gao, X. Wang, J. Chen, Y. Zhou and E. Nishibori, Extraordinary Thermoelectric Performance in MgAgSb Alloy with Ultralow Thermal Conductivity, *Nano Energy*, 2019, **59**, 311–320, DOI: 10.1016/j.nanoen.2019.02.045.

42 D. Li, H. Zhao, S. Li, B. Wei, J. Shuai, C. Shi, X. Xi, P. Sun, S. Meng, L. Gu, Z. Ren and X. Chen, Atomic Disorders Induced by Silver and Magnesium Ion Migrations Favor High Thermoelectric Performance in A-MgAgSb-Based Materials, *Adv. Funct. Mater.*, 2015, **25**(41), 6478–6488, DOI: 10.1002/adfm.201503022.

43 S. Li, J. Yang, Y. Liu, J. Xin, S. Li, Q. Long and Q. Jiang, Enhanced Thermoelectric Properties in MgAgSb Composite with Ag 3 Sb Fabricated by the Microwave-Assisted Process and Subsequent Spark Plasma Sintering, *Adv. Appl. Ceram.*, 2020, **119**(2), 107–113, DOI: 10.1080/17436753.2019.1705018.

44 Z. Liu, J. Shuai, J. Mao, Y. Wang, Z. Wang, W. Cai, J. Sui and Z. Ren, Effects of Antimony Content in MgAg0.97Sbx on Output Power and Energy Conversion Efficiency, *Acta Mater.*, 2016, **102**, 17–23, DOI: 10.1016/j.actamat.2015.09.033.

45 Z. Liu, Y. Wang, J. Mao, H. Geng, J. Shuai, Y. Wang, R. He, W. Cai, J. Sui and Z. Ren, Lithium Doping to Enhance Thermoelectric Performance of MgAgSb with Weak Electron–Phonon Coupling, *Adv. Energy Mater.*, 2016, **6**(7), 1502269, DOI: 10.1002/aenm.201502269.

46 Z. Liu, Y. Zhang, J. Mao, W. Gao, Y. Wang, J. Shuai, W. Cai, J. Sui and Z. Ren, The Microscopic Origin of Low Thermal Conductivity for Enhanced Thermoelectric Performance of Yb Doped MgAgSb, *Acta Mater.*, 2017, **128**, 227–234, DOI: 10.1016/j.actamat.2017.02.015.

47 J. Shuai, H. S. Kim, Y. Lan, S. Chen, Y. Liu, H. Zhao, J. Sui and Z. Ren, Study on Thermoelectric Performance by Na Doping in Nanostructured Mg1-Na Ag0.97Sb0.99, *Nano Energy*, 2015, **11**, 640–646, DOI: 10.1016/j.nanoen.2014.11.027.

48 J. Sui, J. Shuai, Y. Lan, Y. Liu, R. He, D. Wang, Q. Jie and Z. Ren, Effect of Cu Concentration on Thermoelectric Properties of Nanostructured P-Type MgAg0.97−Cu Sb0.99, *Acta Mater.*, 2015, **87**, 266–272, DOI: 10.1016/j.actamat.2015.01.018.

49 X. Tan, L. Wang, H. Shao, S. Yue, J. Xu, G. Liu, H. Jiang and J. Jiang, Improving Thermoelectric Performance of A-MgAgSb by Theoretical Band Engineering Design, *Adv. Energy Mater.*, 2017, **7**(18), 1700076, DOI: 10.1002/aenm.201700076.

50 S. Y. Back, S. Meikle and T. Mori, Comprehensive Study of α-MgAgSb: Microstructure, Carrier Transport Properties, and Thermoelectric Performance under Ball Milling Techniques, *J. Mater. Sci. Technol.*, 2025, **227**, 57–66, DOI: 10.1016/j.jmst.2024.11.061.

51 D. Kraemer, J. Sui, K. McEnaney, H. Zhao, Q. Jie, Z. F. Ren and G. Chen, High Thermoelectric Conversion Efficiency of MgAgSb-Based Material with Hot-Pressed Contacts, *Energy Environ. Sci.*, 2015, **8**(4), 1299–1308, DOI: 10.1039/C4EE02813A.

52 P. Ying, R. He, J. Mao, Q. Zhang, H. Reith, J. Sui, Z. Ren, K. Nielsch and G. Schierning, Towards Tellurium-Free Thermoelectric Modules for Power Generation from Low-Grade Heat, *Nat. Commun.*, 2021, **12**(1), 1–6, DOI: 10.1038/s41467-021-21391-1.

53 P. Ying, L. Wilkens, H. Reith, N. P. Rodriguez, X. Hong, Q. Lu, C. Hess, K. Nielsch and R. He, A Robust Thermoelectric Module Based on MgAgSb/Mg 3 (Sb,Bi) 2 with a Conversion Efficiency of 8.5% and a Maximum Cooling of 72 K, *Energy Environ. Sci.*, 2022, **15**(6), 2557–2566, DOI: 10.1039/D2EE00883A.

54 X. Zhang, H. Zhu, X. Dong, Z. Fan, Y. Yao, N. Chen, J. Yang, K. Guo, J. Hao, L. He, G. Li and H. Zhao, High-Performance MgAgSb/Mg3(Sb,Bi)2-Based Thermoelectrics with $\eta = 12\%$ at $T \leq 583K$, *Joule*, 2024, **8**(12), 3324–3335, DOI: 10.1016/j.joule.2024.08.013.

55 R. He, G. Schierning and K. Nielsch, Thermoelectric Devices: A Review of Devices, Architectures, and Contact Optimization, *Adv. Mater. Technol.*, 2018, **3**(4), 1700256, DOI: 10.1002/admt.201700256.

56 M. T. Agne, K. Imasato, S. Anand, K. Lee, S. K. Bux, A. Zevalkink, A. J. E. Rettie, D. Y. Chung, M. G. Kanatzidis and G. J. Snyder, Heat Capacity of Mg3Sb2, Mg3Bi2, and Their Alloys at High Temperature, *Mater. Today Phys.*, 2018, **6**, 83–88, DOI: 10.1016/j.mtphys.2018.10.001.

57 J. P. Heremans and J. Martin, Thermoelectric Measurements, *Nat. Mater.*, 2024, **23**(1), 18–19, DOI: 10.1038/s41563-023-01726-7.

58 K. A. Borup, J. de Boor, H. Wang, F. Drymiotis, F. Gascoin, X. Shi, L. Chen, M. I. Fedorov, E. Müller, B. B. Iversen and G. J. Snyder, Measuring Thermoelectric Transport Properties of Materials, *Energy Environ. Sci.*, 2015, **8**(2), 423–435, DOI: 10.1039/C4EE01320D.

59 T.-R. Wei, M. Guan, J. Yu, T. Zhu, L. Chen and X. Shi, How to Measure Thermoelectric Properties Reliably, *Joule*, 2018, **2**(11), 2183–2188, DOI: 10.1016/j.joule.2018.10.020.

60 B. R. T. Frost, G. V. Raynor and W. Hume-Rothery, The System Silver-Magnesium-Antimony, with Reference to the Theory of Alloy Formation, *Proc. R. Soc. Lond. A Math. Phys. Sci.*, 1997, **203**(1072), 132–147, DOI: 10.1098/rspa.1950.0130.

61 A. Duparchy, L. Millerand, J. Camut, S. Tumminello, H. Kamila, R. Deshpande, A. Cowley, E. Mueller and J. de Boor, Establishing Synthesis–Composition–Property Relationships for Enhanced and Reproducible Thermoelectric Properties of MgAgSb, *J. Mater. Chem. A*, 2022, **10**(40), 21716–21726, DOI: 10.1039/D2TA05936C.

62 Q. Jiang, J. Yang, P. Hing and H. Ye, Recent Advances, Design Guidelines, and Prospects of Flexible Organic/Inorganic Thermoelectric Composites, *Mater. Adv.*, 2020, **1**(5), 1038–1054, DOI: 10.1039/D0MA00278J.

63 W. W. Scanlon, Precipitation of Te and Pb in PbTe Crystals, *Phys. Rev.*, 1962, **126**(2), 509–513, DOI: 10.1103/PhysRev.126.509.

64 A. H. Adekoya and G. J. Snyder, Thermodynamic Modeling of Bi2Te3 in the Defect Energy Formalism, *Mater. Today Electron.*, 2024, **9**, 100109, DOI: 10.1016/j.mtelec.2024.100109.

65 Z. Zhou, G. Han, X. Lu, G. Wang and X. Zhou, High-Performance Magnesium-Based Thermoelectric Materials: Progress and Challenges, *J. Magnesium Alloys*, 2022, **10**(7), 1719–1736, DOI: 10.1016/j.jma.2022.05.021.

66 L. You, J. Zhang, S. Pan, Y. Jiang, K. Wang, J. Yang, Y. Pei, Q. Zhu, M. T. Agne, G. J. Snyder, Z. Ren, W. Zhang and J. Luo, Realization of Higher Thermoelectric Performance by Dynamic Doping of Copper in N-Type PbTe, *Energy Environ. Sci.*, 2019, **12**(10), 3089–3098, DOI: 10.1039/C9EE01137D.

67 Y. Pei, A. F. May and G. J. Snyder, Self-Tuning the Carrier Concentration of PbTe/Ag2Te Composites with Excess Ag for High Thermoelectric Performance, *Adv. Energy Mater.*, 2011, **1**(2), 291–296, DOI: 10.1002/aenm.201000072.

68 Y. Yu, C. Zhou, X. Zhang, L. Abdellaoui, C. Doberstein, B. Berkels, B. Ge, G. Qiao, C. Scheu, M. Wuttig, O. Cojocaru-Mirédin and S. Zhang, Dynamic Doping and Cottrell Atmosphere Optimize the Thermoelectric Performance of N-Type PbTe over a Broad Temperature Interval, *Nano Energy*, 2022, **101**, 107576, DOI: 10.1016/j.nanoen.2022.107576.

69 S. D. Kang, S. A. Danilkin, U. Aydemir, M. Avdeev, A. Studer and G. J. Snyder, Apparent Critical Phenomena in the Superionic Phase Transition of Cu2-XSe, *New J. Phys.*, 2016, **18**(1), 13024, DOI: 10.1088/1367-2630/18/1/013024.

70 G. J. Snyder, A. H. Snyder, M. Wood, R. Gurunathan, B. H. Snyder and C. Niu, Weighted Mobility, *Adv. Mater.*, 2020, **32**(25), 2001537, DOI: 10.1002/adma.202001537.

71 H.-S. Kim, Z. M. Gibbs, Y. Tang, H. Wang and G. J. Snyder, Characterization of Lorenz Number with Seebeck Coefficient Measurement, *APL Mater.*, 2015, **3**(4), 41506, DOI: 10.1063/1.4908244.

72 Z. Liu, Y. Wang, W. Gao, J. Mao, H. Geng, J. Shuai, W. Cai, J. Sui and Z. Ren, The Influence of Doping Sites on Achieving Higher Thermoelectric Performance for Nanostructured α-MgAgSb, *Nano Energy*, 2017, **31**, 194–200, DOI: 10.1016/j.nanoen.2016.11.010.

73 G. Li, J. Li, L. Zhao, J. Feng and R. Liu, Thermoelectric Performance Enhancement of Pb-Doped α-MgAgSb near Room Temperature, *Appl. Phys. Lett.*, 2024, **124**(18), 183901, DOI: 10.1063/5.0202713.

74 Y. Pei, H. Wang and G. J. Snyder, Band Engineering of Thermoelectric Materials, *Adv. Mater.*, 2012, **24**(46), 6125–6135, DOI: 10.1002/adma.201202919.

75 C. Y. Sheng, H. J. Liu, D. D. Fan, L. Cheng, J. Zhang, J. Wei, J. H. Liang, P. H. Jiang and J. Shi, Predicting the Optimized Thermoelectric Performance of MgAgSb, *J. Appl. Phys.*, 2016, **119**(19), 195101, DOI: 10.1063/1.4949479.

76 Y. Huang, J. Lei, H. Chen, Z. Zhou, H. Dong, S. Yang, H. Gao, T.-R. Wei, K. Zhao and X. Shi, Intrinsically High Thermoelectric Performance in Near-Room-Temperature α-MgAgSb Materials, *Acta Mater.*, 2023, **249**, 118847, DOI: 10.1016/j.actamat.2023.118847.

77 J. Lei, D. Zhang, W. Guan, Z. Cheng, C. Wang and Y. Wang, Engineering Electrical Transport in α-MgAgSb to Realize High Performances near Room Temperature, *Phys. Chem. Chem. Phys.*, 2018, **20**(24), 16729–16735, DOI: 10.1039/C8CP02186D.

78 W. Liu, Q. Jie, H. S. Kim and Z. Ren, Current Progress and Future Challenges in Thermoelectric Power Generation: From Materials to Devices, *Acta Mater.*, 2015, **87**, 357–376, DOI: 10.1016/j.actamat.2014.12.042.

79 Y. Zheng, Q. Zhang, X. Su, H. Xie, S. Shu, T. Chen, G. Tan, Y. Yan, X. Tang, C. Uher and G. J. Snyder, Mechanically Robust BiSbTe Alloys with Superior Thermoelectric Performance: A Case Study of Stable Hierarchical Nanostructured Thermoelectric Materials, *Adv. Energy Mater.*, 2015, **5**(5), 1401391, DOI: 10.1002/aenm.201401391.

80 L. Qian, M. Li, Z. Zhou, H. Yang and X. Shi, Comparison of Nano-Indentation Hardness to Microhardness, *Surf. Coat. Technol.*, 2005, **195**(2), 264–271, DOI: 10.1016/j.surfcoat.2004.07.108.

81 G. Li, K. R. Gadelrab, T. Souier, P. L. Potapov, G. Chen and M. Chiesa, Mechanical Properties of BixSb2−xTe3 Nanostructured Thermoelectric Material, *Nanotechnology*, 2012, **23**(6), 65703, DOI: 10.1088/0957-4484/23/6/065703.

82 G. Rogl, A. Grytsiv, M. Gürth, A. Tavassoli, C. Ebner, A. Wünschek, S. Puchegger, V. Soprunyuk, W. Schranz, E. Bauer, H. Müller, M. Zehetbauer and P. Rogl, Mechanical Properties of Half-Heusler Alloys, *Acta Mater.*, 2016, **107**, 178–195, DOI: 10.1016/j.actamat.2016.01.031.

83 C. Lee, P. Dharmaiah, D. H. Kim, D. K. Yoon, T. H. Kim, S. H. Song and S.-J. Hong, Synergistic Optimization of the Thermoelectric and Mechanical Properties of Large-Size Homogeneous Bi0.5Sb1.5Te3 Bulk Samples via Carrier Engineering for E cient Energy Harvesting, *ACS Appl. Mater. Interfaces*, 2022, **14**(8), 10394–10406, DOI: 10.1021/acsami.1c23736.

84 B. Li, P. Xie, S. Zhang and D. Liu, Lead Germanium Telluride: A Mechanically Robust Infrared High-Index Layer, *J. Mater. Sci.*, 2011, **46**(11), 4000–4004, DOI: 10.1007/s10853-011-5327-9.

85 R. D. Schmidt, E. D. Case, L.-D. Zhao and M. G. Kanatzidis, Mechanical properties of low-cost, earth-abundant chalcogenide thermoelectric materials, PbSe and PbS, with additions of 0–4% CdS or ZnS, *J. Mater. Sci.*, 2015, **50**(5), 1770–1782, DOI: 10.1007/s10853-014-8740-z.

86 Y.-X. Zhang, Y.-K. Zhu, J. Feng and Z.-H. Ge, Precious Metal Nanoparticles Dispersing toward Highly Enhanced Mechanical and Thermoelectric Properties of Copper Sulfides, *J. Alloys Compd.*, 2022, **892**, 162035, DOI: 10.1016/j.jallcom.2021.162035.

87 P. Dharmaiah, M. Heo, C. Nagarjuna, S.-J. Jung, S. O. Won, K. H. Lee, S. K. Kim, J.-S. Kim, B. Ahn, H.-S. Kim and S.-H. Baek, Enhancement of Thermoelectric Properties in P-Type ZnSb Alloys through Cu-Doping, *J. Alloys Compd.*, 2024, **1004**, 175739, DOI: 10.1016/j.jallcom.2024.175739.

88 T. Dahal, S. Gahlawat, Q. Jie, K. Dahal, Y. Lan, K. White and Z. Ren, Thermoelectric and Mechanical Properties on Misch Metal Filled P-Type Skutterudites Mm0.9$Fe_{4-x}Co_xSb12$, *J. Appl. Phys.*, 2015, **117**(5), 55101, DOI: 10.1063/1.4906954.

